Anomalous Shubnikov-de Haas quantum oscillations in rare-earth tritelluride NdTe₃

Kirstine J. Dalgaard [1,*] Shiming Lei [2] Steffen Wiedmann [3] Martin Bremholm,[1] and Leslie M. Schoop [2,†]

[1]*Department of Chemistry and Interdisciplinary Nanoscience Center, Aarhus University, Aarhus, Denmark*
[2]*Department of Chemistry, Princeton University, Princeton, New Jersey 08544, USA*
[3]*High Field Magnet Laboratory (HFML-EMFL), Radboud University, Nijmegen, Netherlands*

Materials with the structural motif of a square net have in recent years attracted attention for their often unexpected electronic properties. Here, we present low-temperature magnetotransport experiments on high-quality NdTe₃ single crystals with a carrier mobility of 6×10^4 cm²/V s at 2.25 K; an increase of 58% is observed below the Néel temperature. Shubnikov-de Haas oscillations up to 9 T exhibit anomalies in their amplitude which deviates from the conventional Lifshitz-Kosevich behavior below the magnetic ordering temperature and around 20 K. The latter, which has so far not been observed in any tritelluride, suggests a field- and temperature-induced electronic structure transition. We provide a thorough analysis of three different samples, highlighting the importance of sample quality for elucidating details in the transport behavior. Our results on NdTe₃ suggest that rare-earth tritellurides may display so-far obscured exotic electronic properties in addition to the well-studied high-temperature charge density wave anomalies.

I. INTRODUCTION

Delocalized, hypervalent chemical bonds in main-group element square-net materials have recently been linked to the appearance of band inversions and topologically nontrivial band structures [1]. Such chemical bonds can be viewed as directional metallic bonds, where the electrons can move freely in two dimensions, but are confined within the square net. Delocalized chemical bonds most famously appear in graphene, which is known for its high carrier mobility [2,3]. An obvious question is whether this rare type of chemical bonding affects the electronic transport in other materials as well. Previous reports have indeed revealed unusual aspects of materials featuring the structural motif of a square net [4–6]. For example, nodal-line semimetal ZrSiS has been shown to undergo an unconventional mass enhancement of the quasiparticles near the nodal loop and an anomalous temperature dependence of the Shubnikov-de Haas (SdH) oscillation amplitude [7,8]. Similarly, GdTe₃ was recently shown to exhibit remarkably high charge carrier mobility, beyond 6×10^4 cm²/V s, despite its magnetic order [9]. Here, we report a similarly high carrier mobility in the related compound NdTe₃. The mobility in NdTe₃ is enhanced below the magnetic-ordering temperature, due to the reduction in spin-disorder scattering [10]. The fact that the high mobility in rare-earth tritellurides (RTe₃) is not limited to the Gd phase, where f electrons are usually localized well below the Fermi level, opens the possibility for the existence of layered, high-mobility, correlated phases in the rare-earth tritelluride family. In addition, NdTe₃ exhibits peculiar anomalies around 20 K in the temperature-dependent

SdH oscillation amplitude. This feature is highly sample dependent, underpinning the importance of high sample quality and a careful analysis of multiple samples.

RTe₃ phases crystallize in a weakly orthorhombic structure with the space group *Bmmb* (*Cmcm*). The structure [Fig. 1(a)] consists of buckled RTe bilayers that alternate double Te square-net layers, which are held together by van der Waals forces. Te-based square-net materials such as the rare-earth tritellurides have a desire to undergo charge density wave (CDW) transitions, for which they have long been investigated [11–13]. Depending on the rare-earth element R, the RTe₃ compounds host either one (R = Gd, Sm, and lighter) or two (R = Tm, Er, Ho, Dy, Tb) incommensurate CDWs, involving distortions in the Te square net [14,15]. In spite of the CDW(s), the Fermi surface is not fully gapped, and the materials exhibit metallic conductivity down to low temperatures [9,13,14]. While the CDWs in these phases have been reported in detail in the past, less attention has been paid to the low-temperature magnetotransport properties and magnetic quantum oscillations (QOs) of RTe₃, where only a limited number of studies exist [9,16–18].

Here, we report the low-temperature transport properties of high-quality NdTe₃ crystals. In addition to the observations of very high mobility and indications of a temperature-induced Lifshitz transition, we also provide a thorough analysis of different samples, highlighting the importance of sample quality for transport studies in these systems. Apart from a high residual resistivity ratio *RRR*, the high quality is manifested as the onset of QOs at low field, large magnetoresistance *MR* at high field, and large Hall mobility. Many features reported here may have been hidden in previous QO studies of lower quality samples. The QO study presented herein includes de Haas-van Alphen (dHvA) as well as SdH oscillations and resolves, to the best of our knowledge, the most details of

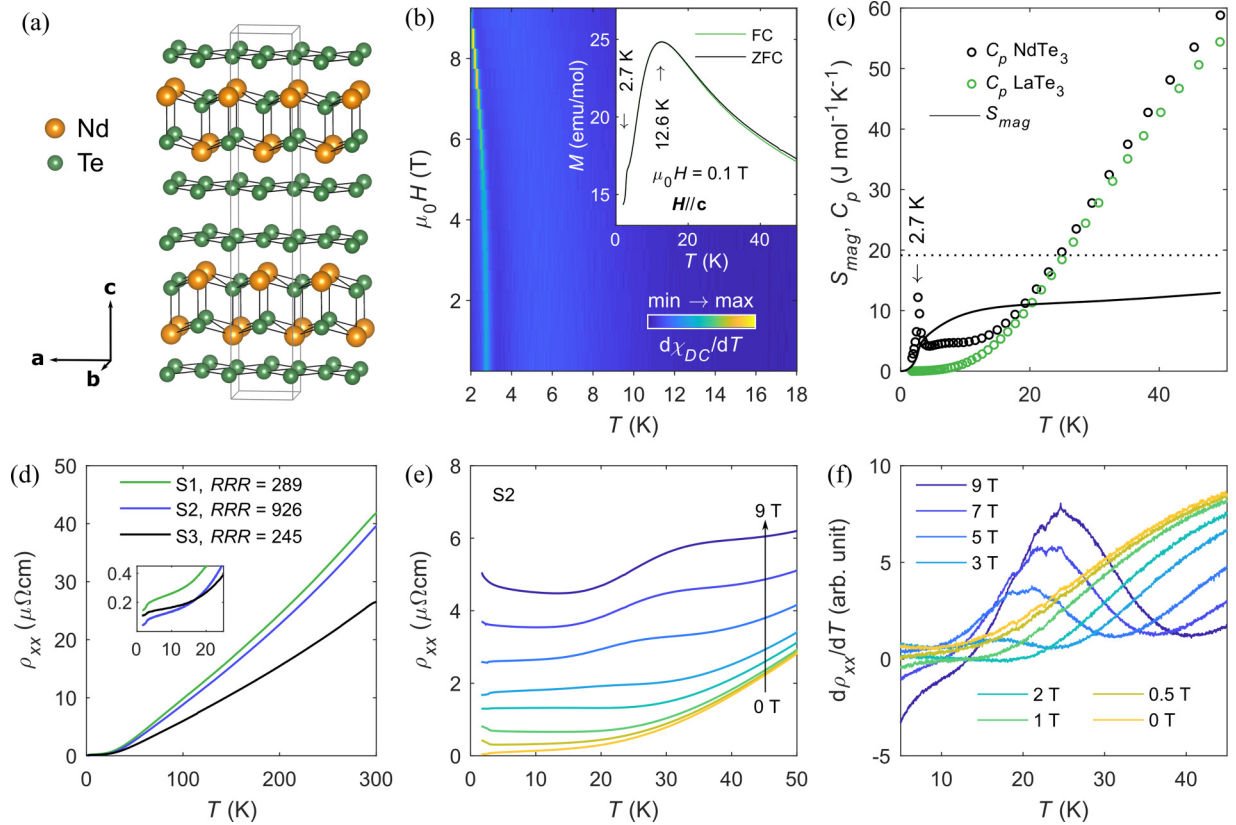*kjd@inano.au.dk
†lschoop@princeton.edu

FIG. 1. (a) Average atomic structure of $NdTe_3$ in the *Bmmb* setting. The box indicates the unit cell without considering the CDW. (b) Color map showing the temperature derivative of the magnetic susceptibility $\chi_{DC} = M/\mu_0 H$ as a function of temperature and field strength, with the field direction parallel to the crystallographic c axis. The map illustrates the decreasing trend of T_N, as the field strength is increased. Inset: Temperature-dependent [field-cooled (FC) and zero-field-cooled (ZFC)] magnetization at a constant applied field of 0.1 T parallel to the crystallographic c axis. (c) Specific heat C_p of $NdTe_3$ and nonmagnetic $LaTe_3$ and the calculated magnetic entropy S_{mag}. The dashed line is $R\ln(2J + 1)$, the expected magnetic entropy based on the number of unpaired electrons. (d) Temperature-dependent resistivity at zero field for three samples, S1, S2, and S3. The inset shows a zoom of the plot at low temperature. (e) Temperature-dependent resistivity at nonzero field for S2 and (f) its temperature derivative.

the Fermi surface on a rare-earth tritelluride, albeit being conducted in low fields.

II. METHODS

A. Experimental

Single crystals of $NdTe_3$ were grown by a self-flux method with excess of tellurium. Te (>99.999%; Sigma-Aldrich) was first purified and then mixed with neodymium (>99.9%; Sigma-Aldrich) in a ratio of 97 : 3. The mixed raw materials were sealed in an evacuated quartz ampule and heated to 900 °C over the duration of 12 h, and then slowly cooled down to 550 °C at a rate of 2 °C/h. The Te flux was separated from the crystals by a centrifuging process. We also prepared samples with an additional annealing step, where crystals inside an evacuated quartz tube were placed in a tube furnace with the hot end and cold end at 410 °C and 360 °C, respectively. This way, the residual Te flux is removed from the crystal surface by vapor transport. In this work, we provide transport measurements on samples before (S1 and S2) and after (S3) annealing.

Transport measurements were carried out in a Quantum Design PPMS DynaCool system, using the electrical transport option. The electrical contacts were made with Ti (15 nm)/Au (50 nm) connected with conductive silver paste and thin gold wire. The longitudinal resistivity was measured in a standard four-terminal geometry with a constant alternating current of 5 mA for all samples. The Hall data were obtained in a conventional Hall effect measurement geometry. For further analysis, the Hall resistivity and longitudinal resistivity were antisymmetrized and symmetrized, respectively, in field B by taking advantage of two measurements with the magnetic field in opposite directions. The probed samples were thin exfoliated crystals with thicknesses of 8 μm (S1), 16 μm (S2), and 10 μm (S3).

The temperature-dependent DC magnetization and AC magnetic susceptibility were measured on a Quantum Design PPMS DynaCool system via the vibrating sample magnetometer (VSM) option and the ACMS option, respectively. For these measurements, a crystal of 15.2 mg from the same batch as the transport sample S1 was used.

The chemical composition of $NdTe_3$ was analyzed by energy-dispersive x-ray spectroscopy using a Verios 460 scanning electron microscope with an Oxford energy-dispersive x-ray spectrometer and with incident electron energy of 15 keV. These data are found in the Supplemental Material

(SM) [19]. Heat capacity measurements were performed by the relaxation method on a Quantum Design PPMS DynaCool system. Data on LaTe$_3$ and NdTe$_3$ were collected at zero magnetic field.

B. Data analysis

The oscillating part of the longitudinal resistivity ρ was extracted by taking the derivative with respect to inverse field B^{-1} and subtracting a slowly varying polynomial background. The oscillations were described by the dominating part of the first derivative of the Lifshitz-Kosevich (L-K) expression,

$$\Delta \frac{d\rho}{d\left(\frac{1}{B}\right)} \propto -\frac{\lambda T}{\sinh(\lambda T)} e^{-\lambda T_D} \sin\left[2\pi\left(\frac{F}{B} - \frac{1}{2} + \beta + \delta\right)\right], \quad (1)$$

where $\lambda = 2\pi^2 k_B m^*/(\hbar e B)$, k_B is the Boltzmann constant, $\hbar$ is the reduced Planck constant, m^* is the cyclotron mass, T_D is the Dingle temperature, T is the temperature, and F is the oscillation frequency. $2\pi\beta$ is the Berry phase and δ is a phase shift equal to 0 for 2D systems or $\pm\frac{1}{8}$ for 3D systems. The quantum mobility μ_q can be extracted from fitted parameters, as $\mu_q = e\hbar/(2\pi k_B m^* T_D)$.

The temperature-dependent oscillation amplitude at a fixed field value was described by the L-K temperature reduction factor

$$R_T = \frac{\lambda T}{\sinh(\lambda T)} \quad (2)$$

to extract the cyclotron mass. The SdH oscillation amplitudes were determined through the following procedure: First, a fast Fourier transform (FFT) revealed the frequencies in the oscillation patterns. With this knowledge, the sum of an appropriate number of damped oscillating functions was fitted to the pattern, to extract the individual amplitude(s). This was done for all temperatures, and the temperature reduction factor R_T was then fitted to the temperature-dependent amplitudes to extract the cyclotron mass for each pocket in question. The obtained cyclotron mass(es) were then used in a L-K fit with Eq. (1) to the SdH oscillations to extract the Dingle temperature and quantum mobility for each Fermi pocket in question.

DHvA oscillations were analyzed in a similar fashion, following the procedure outlined in Ref. [9] and elaborated in the SM [19].

The transport carrier mobilities μ_e and μ_h and carrier concentrations n_e and n_h of electrons and holes, respectively, were determined from the Hall resistivity through a two-band model,

$$\rho_{yx}(B) = \frac{B}{e} \frac{(n_h\mu_h^2 - n_e\mu_e^2) + (n_h - n_e)(\mu_e\mu_h B)^2}{(n_e\mu_e + n_h\mu_h)^2 + (n_h - n_e)^2(\mu_e\mu_h B)^2}, \quad (3)$$

with the constraint that the zero-field resistivity is related to the carrier mobility and concentration through

$$\rho_{xx}(0) = \frac{1}{e} \frac{1}{n_e\mu_e + n_h\mu_h}, \quad (4)$$

where $B = \mu_0 H$, μ_0 is the free-space permeability, and e is the elementary charge. Fits to the Hall conductivity were also performed, following the procedure outlined in Ref. [9].

III. RESULTS AND DISCUSSION

A. Magnetism

Temperature- and field-dependent phase transitions in a bulk NdTe$_3$ single crystal were explored through magnetization M and heat capacity C_p measurements, as illustrated in Figs. 1(b) and 1(c). A magnetic phase transition, referred to as the Néel transition, occurs at $T_N = 2.7$ K at zero field, in agreement with previous measurements [20,21]. The transition is also visible in the resistivity at zero field [Fig. 1(d), inset]. The Néel temperature decreases gradually to about 2.0 K as the external field approaches 9 T, as illustrated by the map in Fig. 1(b) of the temperature derivative of $\chi_{DC} = M/\mu_0 H$. The shape and magnitude of the out-of-plane magnetization [Fig. 1(b), inset] is in good agreement with what has previously been reported for this compound [21]. The authors also demonstrated a large anisotropy of the out-of-plane and in-plane magnetization and concluded that the magnetic moments are oriented in the *ab* plane in the ordered state.

As in the previous study [21], we also observe a broad maximum at 12.6 K [Fig. 1(b), inset], which was previously attributed to the crystal field effect and the existence of a small component of the magnetic moment along the *c* axis for the ground-state 4f level above T_N.

The signature of the crystal field effect is also revealed in the heat capacity measurement. The magnetic contribution can be reasonably extracted by taking advantage of the nonmagnetic analog, LaTe$_3$. The magnetic entropy [Fig. 1(c)] reaches only 68% of the theoretical value of $R\ln10$ for a 10-fold-degenerate ground multiplet, and the magnetic entropy fails to saturate up to 50 K. This is due to the crystal field effect, which lifts the degeneracy and results in a much lower magnetic entropy at the ordering temperature. A similar signature of the crystal field effect has been revealed in CeTe$_2$, PrTe$_2$, and SmTe$_2$ [22].

The temperature-dependent resistivity $\rho_{xx}(T)$ was measured for three samples, referred to as S1 ($RRR = 289$), S2 ($RRR = 926$), and S3 ($RRR = 245$), where the $RRR = \rho(300\text{ K})/\rho(1.7\text{ K})$ is obtained from the temperature-dependent resistivity at zero field [Fig. 1(d)]. The high residual resistivity ratio indicates high crystal quality for all three samples. Particularly, the RRR of 926 in S2 is the highest reported among RTe$_3$ systems, to the best of our knowledge. Below T_N the resistivity drops, which is a common feature of magnetic materials due to the loss of spin-disorder scattering [23,24]. Above T_N, an additional anomaly is observed in $\rho_{xx}(T)$, when an external magnetic field of more than 2 T is applied [Fig. 1(e)]. This feature is better visualized in the derivative in Fig. 1(f). Above 2 T, the anomaly emerges as a broad peak in $d\rho_{xx}/dT$ with a clear temperature and field dependence: the peak intensity increases and the peak position moves to higher temperature with larger field strength. The characteristics of the anomaly has an interesting similarity to those reported for the second CDW transition in the RTe$_3$ compounds with heavier rare-earth elements [14]. Furthermore, the same features were also observed recently for the nonmagnetic LaTe$_3$ [25]. Based on their experiments and band structure calculations, the authors suggested an additional CDW transition induced by a magnetic field at low temperature. This resemblance with LaTe$_3$ suggests a
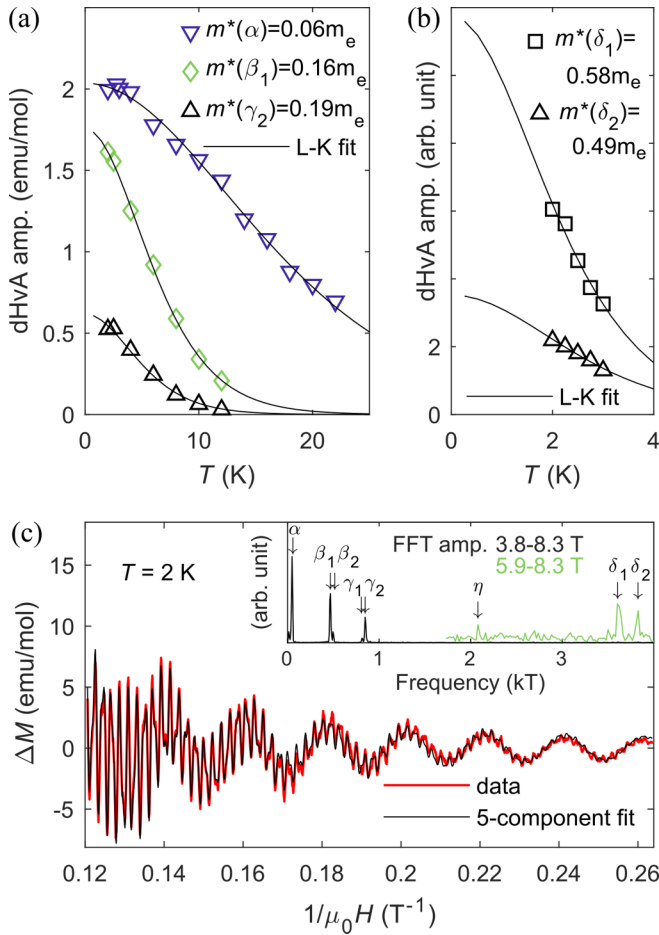
FIG. 2. L-K analysis of QOs in the DC magnetization. (a) Temperature-dependent dHvA oscillation amplitude of the α, β_1, and γ_2 frequencies at 6.4 T. (b) Temperature-dependent dHvA oscillation amplitude of the δ_1 and δ_2 frequencies, obtained from a FFT of the field range, 7.55–9 T. The cyclotron masses were extracted by fitting the L-K temperature reduction factor. (c) DHvA oscillations in the magnetization at 2 K. The inset shows the FFT of two different field ranges (not plotted at the same scale).

nonmagnetic origin of the feature in NdTe$_3$ as well. In addition to the clear anomaly observed in the temperature-dependent resistivity, we further observe a deviation from the L-K behavior by the SdH oscillation amplitude in the same temperature range, as discussed in the following section. Such a feature was not observed in LaTe$_3$, since quantum oscillations were not observed in Ref. [25], nor has this feature been reported for any other RTe$_3$ before, to the best of our knowledge.

B. Quantum oscillations

SdH as well as dHvA oscillations starting at 2 T or below were recorded for the NdTe$_3$ samples, indicating high crystal quality and low-mass, high-mobility carriers. A FFT of the dHvA oscillations reveals seven main frequencies, α, $\beta_{1,2}$, $\gamma_{1,2}$, and $\delta_{1,2}$ (Figs. 2 and 3). Additionally, it reveals a weak high-frequency oscillation η. These quantum oscillation frequencies are similar to those of GdTe$_3$ [9], suggesting a similar Fermi surface geometry. Among the dHvA frequencies, $\beta_{1,2}$ and $\gamma_{1,2}$ can be assigned to electron pockets around the X point, which are unaffected by the CDW, whereas the remaining frequencies are likely a result of a CDW-induced Fermi surface reconstruction [9,26]. A L-K analysis was applied to the dHvA oscillations in the DC magnetization as well as the AC magnetic susceptibility, and the results are summarized in Table I. Further details and discussion are given in Sec. SIII of the SM [19].

In the transport measurements, the small α frequency of 35–50 T is well resolved, while the β, γ, and η oscillations have much weaker amplitudes. Note that the dHvA measurements were performed on a crystal from the same batch as the transport sample S1. In the remainder of the section we focus on transport measurements, starting with the samples, S2 and S3, with the higher crystal quality to explore the properties of the remarkably small α pocket. In percentage of the Brillouin-zone cross-sectional area $a^*b^* = 2.09$ Å^{-2} where $a = b = 4.35$ Å [27], the α pocket amounts to 0.2%. Furthermore, we resolve here that α consists of at least two frequencies.
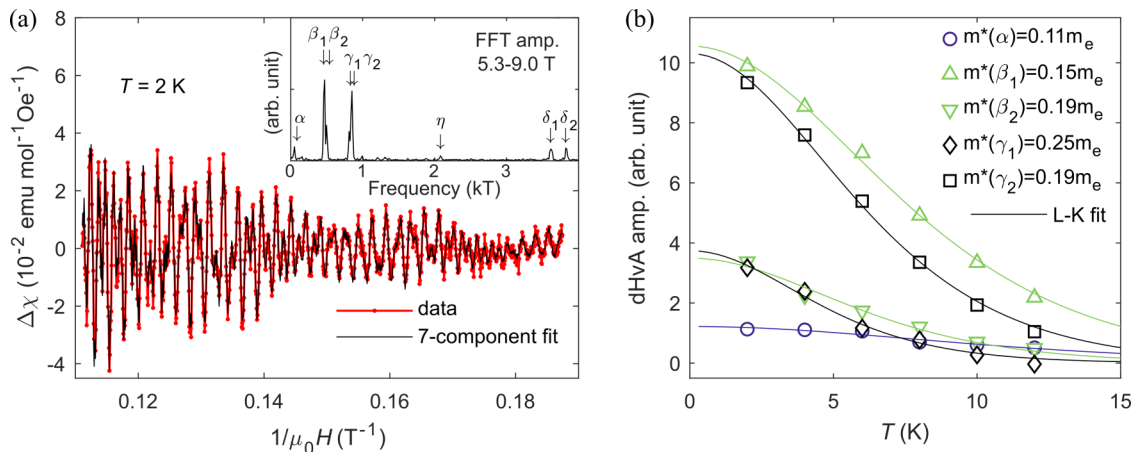

FIG. 3. L-K analysis of QOs in the AC magnetic susceptibility. (a) DHvA oscillations at 2 K. The inset shows the FFT. (b) Temperature-dependent dHvA oscillation amplitude of the α, β, and γ frequencies at 7.8 T. The cyclotron masses m^* were extracted by fitting the L-K temperature reduction factor (solid lines matched by color to the data points).

TABLE I. Parameters from the L-K analysis of dHvA oscillations at 2 K. The corresponding fits are given in Fig. 2(c) and Fig. 3(a). The cyclotron masses for the β_2 and γ_1 oscillations marked with an asterisk (*) were calculated from the magnetic susceptibility $\chi_{AC} = dM/dB$. The cyclotron masses for δ_1 and δ_2 oscillations, marked with two asterisks (**) were calculated from the magnetization M.

Pocket	F (T)	m^* (m_e)	T_D (K)	μ_q (cm^2/V s)
		dHvA (DC magnetization)		
α	50	0.06(1)	4(2)	$9(2) \times 10^3$
β_1	468	0.16(1)	12(1)	$1.17(3) \times 10^3$
β_2	503	0.19(6)*	11(3)	$0.99(3) \times 10^3$
γ_1	810	0.25(4)*	6(1)	$1.45(7) \times 10^3$
γ_2	850	0.19(2)	9(1)	$1.26(1) \times 10^3$
η	2.1×10^3	NA	NA	NA
δ_1	3.6×10^3	0.6(2)	NA	NA
δ_2	3.8×10^3	0.5(2)	NA	NA
		dHvA (AC magnetic susceptibility)		
α	50	0.11(2)	NA	NA
β_1	467	0.15(3)	16(4)	867(5)
β_2	499	0.19(6)	6(2)	$1.8(1) \times 10^3$
γ_1	810	0.25(4)	7(2)	$1.20(2) \times 10^3$
γ_2	850	0.19(2)	16(1)	718(5)
η	2.1×10^3	NA	NA	NA
δ_1	3620	0.6(2)**	7(2)	$0.51(1) \times 10^3$
δ_2	3830	0.5(2)**	3(2)	$1.8(9) \times 10^3$

SdH oscillations for S2 at selected temperatures between 12 K and 50 K are presented as the first derivative with respect to the inverse magnetic field in Fig. 4(a). The two dashed lines mark the positions of neighboring maxima. For all temperatures, we have performed a FFT analysis. In the temperature range between 1.8 K and 17 K, two frequencies at 35 T and 45 T are present as can be seen in the insets in Fig. 4(c), while above 17 K, only oscillations with the smaller frequency are found.

To extract the cyclotron masses of the quasiparticles in both pockets (α_1 and α_2), the temperature-dependent SdH oscillation amplitudes at $\mu_0 H = 7$ T were extracted by fitting two (1.8–17 K) or one (20–50 K) damped oscillators, with the result given in Fig. 4(b). At this field, the two frequencies interfere constructively. Therefore, the black triangles in Fig. 4(b) should represent the sum of the two individual amplitudes marked by red squares and black circles, respectively, assuming that two components may contribute to the oscillations beyond the temperature where a two-component fit is defensible. Figure 4(c) shows representative fits of the L-K equation [Eq. (1)] to the SdH oscillations at 4 K and 10 K using two components, and at 30 K using one component. The extracted parameters, cyclotron mass, Dingle temperature, and quantum mobility, are given at 4 K in Table II.

From the T-dependent SdH oscillation amplitude, we define three distinct temperature regions (i)–(iii) represented by the color-shaded areas in Fig. 4(b). In region (ii), between 4 and 17 K, the amplitudes follow the conventional L-K behavior. A fit to the data points from 4–14 K using the temperature reduction factor R_T [Eq. (2)] for both frequencies gives
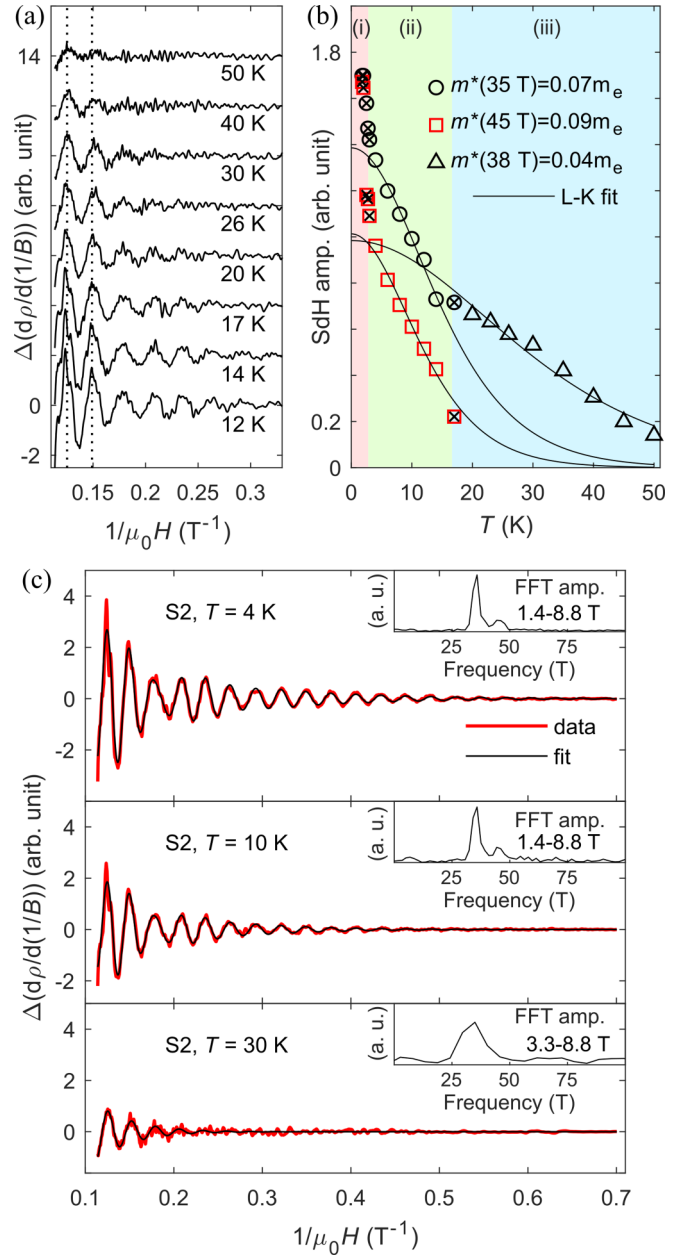

FIG. 4. (a) SdH oscillations of S2 at multiple temperatures. (b) Temperature-dependent SdH oscillation amplitude of S2 at $\mu_0 H = 7.0$ T, obtained from fitting two (red squares and black circles) or one (black triangles) damped oscillators. Cyclotron masses were extracted from L-K fits, where the crossed data points were excluded. In the red-shaded region (i), the system is in the antiferromagnetic state. In the blue-shaded region (iii), the SdH oscillation amplitude deviates from the expected L-K behavior. (c) SdH oscillations with two-component L-K fits at 4 K and 10 K and with a one-component fit at 30 K. The insets show the FFT of the data.

$m^*(35 \text{ T}) = 0.07(1)m_e$ and $m^*(45 \text{ T}) = 0.09(1)m_e$. Above 17 K [region (iii)], we only find oscillations with a frequency of $F = 38$ T, as determined from a fit with a damped oscillator. The temperature reduction factor was fitted to the amplitude in the 20–50 K range as well, giving $m^* = 0.04(1)m_e$. However, it is not clear whether this region is characterized

TABLE II. Parameters from a two-component L-K sum fitted to the SdH quantum oscillations in the three studied samples at 4 K. The corresponding fits are given in Figs. 5(c), 4(c), and 6(c). For each sample, the dominant frequency is labeled α_1.

Sample	Pocket	F (T)	m^* (m_e)	T_D (K)	μ_q (cm^2/V s)
S3 ($RRR = 245$)	α_1	43.0	0.07(1)	9.3(9)	$3.1(3) \times 10^3$
	α_2	45.5		6(1)	$5.3(9) \times 10^3$
S2 ($RRR = 926$)	α_1	35.3	0.07(1)	6(2)	$4.9(3) \times 10^3$
	α_2	45.4	0.09(1)	16(2)	$1.6(2) \times 10^3$
S1 ($RRR = 289$)	α_1	42.3	0.07(1)	14(2)	$2.2(3) \times 10^3$
	α_2	40.1		13(4)	$3(1) \times 10^3$

by one cyclotron mass or perhaps a continuous deformation over the range of temperatures. Below the Néel temperature [region (i)], the amplitude shows an increase, thereby deviating from the conventional L-K behavior. We note that the anomalies described here are very robust against different approaches to extracting the amplitude, as demonstrated in Sec. SII.C of the SM [19].

While the low-temperature increase in the SdH oscillation amplitude occurs exactly at the Néel temperature and can be related to a change in the magnetic order and scattering properties of the system, the high-T transition must have a different origin. Moreover, it is evident that the cyclotron mass is reduced by approximately a factor of two at higher temperatures.

In Fig. 5(a), SdH oscillations of S3 are shown at selected temperatures from 15 K to 40 K. The two dashed lines mark the positions of neighboring maxima at all temperatures up to 18 K. At 21 K and above, the positions of maxima start to shift, such that the second dashed line marks a minimum at 30–40 K. From 21 K to 40 K, the overall frequency undergoes

an increase. This is readily observed in Fig. 5(a) from the distance between neighboring maxima and confirmed when a damped oscillator is fitted to the SdH oscillations.

Furthermore, above 21 K the oscillation amplitude appears to increase slightly with temperature, as opposed to the decrease expected from the L-K temperature reduction factor. The anomalous behavior is confirmed in Fig. 5(b). The amplitudes at $\mu_0 H = 8.5$ T and $\mu_0 H = 6.0$ T were extracted from fitting a single damped oscillator. Although at low temperature the beating pattern and double peak in the FFT [Fig. 5(c)] reveal two close-lying frequencies of 43 T and 46 T, temperature-dependent amplitudes could not reliably be extracted for the two individual frequencies. The beating feature is most pronounced at 4 K and only present up to 9 K.

As was the case for S2, three temperature regions (i)–(iii) can be identified for S3 with deviations from the L-K behavior below the Néel temperature [region (i)], and from 21 K and above [region (iii)]. In the 4–18 K range [region (ii)], the amplitude follows a conventional L-K behavior with $m^* = 0.07(1)m_e$. The fitted cyclotron mass in region (ii) is expected to lie between the real cyclotron masses represented by the two frequencies in the oscillation pattern. Like the anomalies of S2, the anomalies of S3 are robust against different approaches to extracting the amplitude, as demonstrated in Sec. SII.C of the SM [19].

It is worth noting that the anomaly in region (iii) appears to be field dependent as well as temperature dependent with the amplitude minimum at 21 K when $\mu_0 H = 6.0$ T and at 27 K when $\mu_0 H = 8.5$ T. Thus, the feature appears at higher temperature when the field is stronger, which is also the case for the $\rho_{xx}(T)$ anomaly in Figs. 1(e) and 1(f).

As established from Fig. 5(a), the anomaly in the temperature-dependent SdH oscillation amplitude is
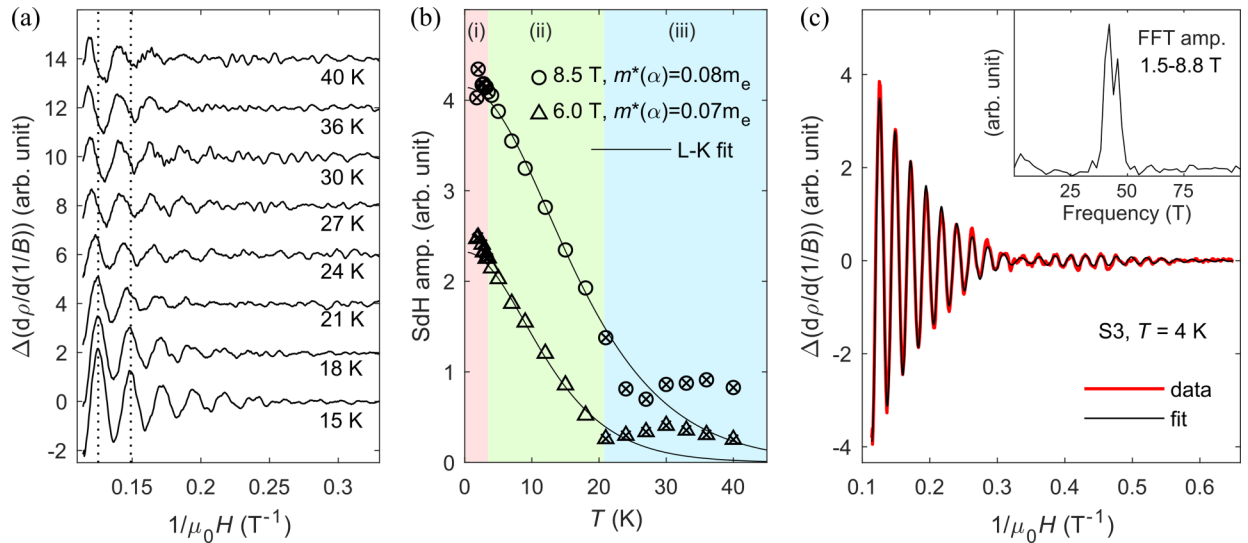

FIG. 5. (a) SdH oscillations of S3 at multiple temperatures. The dashed lines highlight a shift in peak positions, as the temperature is raised. (b) Temperature-dependent SdH oscillation amplitude of S3 at $\mu_0 H = 8.5$ T and $\mu_0 H = 6.0$ T, obtained from fitting a single damped oscillator. The cyclotron mass was extracted from a L-K fit, where the crossed data points were excluded. In the red-shaded region (i), the system is in the antiferromagnetic state. In the blue-shaded region (iii), the SdH oscillation amplitude deviates from the expected L-K behavior. (c) SdH oscillations with a two-component L-K fit at 4 K using $m^* = 0.07m_e$ for both components. The data show a beating pattern with a node at about $\mu_0 H = 3$ T. The inset shows the FFT of the data.
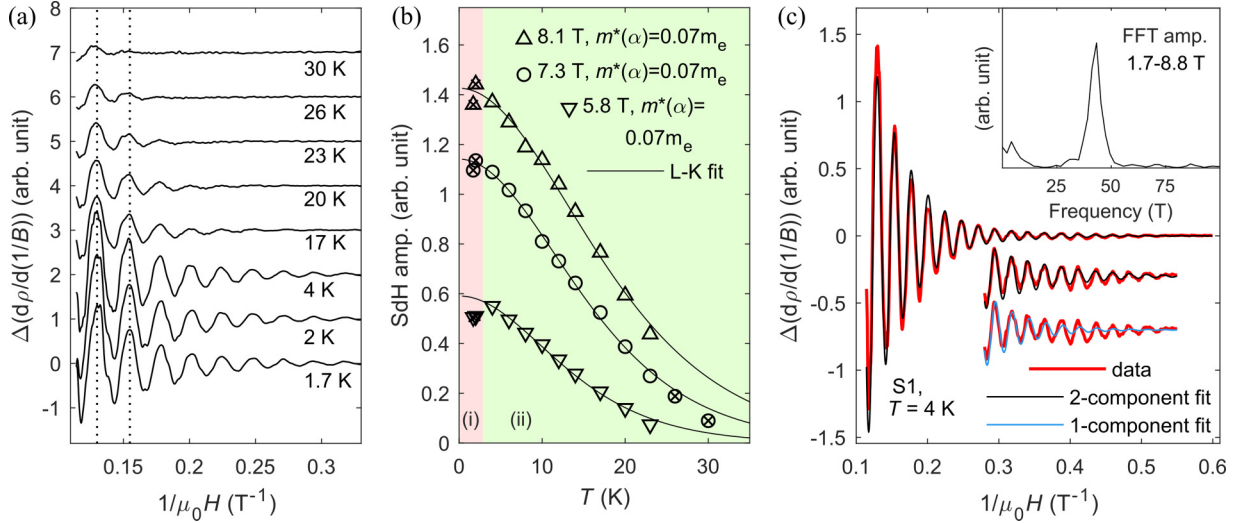
FIG. 6. (a) SdH oscillations of S1 at multiple temperatures. (b) Temperature-dependent SdH oscillation amplitude of S1 at $\mu_0 H = 8.1$ T, $\mu_0 H = 7.3$ T, and $\mu_0 H = 5.8$ T, determined manually from a neighboring peak and valley in the oscillations in $\Delta d\rho/d(1/B)$. The cyclotron mass was extracted from a L-K fit, where the crossed data points were excluded. In the red-shaded region (i) the system is in the antiferromagnetic state. In the green-shaded region (ii) the amplitude follows the conventional L-K behavior. (c) SdH oscillations at 4 K with a two-component L-K fit (black line), using $m^* = 0.07m_e$ for both components. The data plotted with a downward shift are multiplied by 4 to emphasize the improvement of a two-component fit with respect to a single-component fit (blue line). The inset shows the FFT of the data.

accompanied by a gradually increasing frequency. Such a frequency change indicates an increase of the size of the extremal orbit area, and correspondingly the size of the Fermi pocket (cf. the Onsager relation). Altogether, the observations indicate a temperature- and field-induced change of the Fermi surface.

Figure 5(c) shows a representative two-component fit of the L-K equation [Eq. (1)] using $m^* = 0.07m_e$ for both components at 4 K. The fitted parameters are given in Table II.

The last sample, S1, behaves differently compared to S2 and S3 in two ways, as displayed in Fig. 6: First, it does not show an anomaly in the SdH oscillation amplitude above T_N for temperatures up to 30 K. This may be due to the lower crystal quality of this sample, which has the smallest MR at 9 T, the smallest measured Hall mobility, and the highest onset of quantum oscillations among the three samples [19]. Comparing the SdH QO behaviors of S2 and S3, there seems to be an indication that samples with lower quality (S3) would have a higher anomaly onset temperature. In this sense, it is likely that the anomaly in S1 would appear above 30 K where no QOs are visible in our field range. Second, the steep increase of the temperature-dependent oscillation amplitude below the Néel temperature in S3 and S2 is not present in S1. For S1, the two data points below T_N, at 1.7 K and 2 K, have a decreasing or flattening behavior (Fig. 6(b) and Fig. S4 [19]). A similar behavior was observed in GdTe$_3$, where the amplitude remained constant below the Néel temperature at 12 K [9]. This deviation was interpreted as an indication of interplay between magnetic order and electronic transport. This is likely the case in NdTe$_3$ too, and the sample variation suggests competing mechanisms.

The features presented in Fig. 6(b) are robust against different approaches to extracting the amplitude (Sec. SII.C of

the SM [19]). The parameters obtained from applying the L-K analysis to the SdH oscillations of S1 (detailed in Sec. SII.B of the SM [19]) are given in Table II.

While the SdH oscillation amplitude anomalies below the Néel transition are likely connected to the magnetic ordering, the high-temperature anomaly in region (iii) of S2 and S3 does not offer a straightforward interpretation. The temperature-dependent magnetization at zero field shows a broad peak, attributed to some degree of magnetic order, with the maximum at $T = 12.6$ K [Fig. 1(b), inset], which is close to the onset of the deviation from L-K behavior of the temperature-dependent QO amplitude. However, this feature shifts to lower temperatures with increasing applied field, whereas the QO amplitude anomaly in S3 apparently has the opposite field dependence. It is therefore tempting to connect the amplitude anomaly to the anomaly in $\rho_{xx}(T)$ between $\sim$15 K and $\sim$40 K [Figs. 1(e) and 1(f)], which has a similar field and temperature dependence. At this moment, the origin of the anomalous temperature dependence of the SdH oscillation amplitude in NdTe$_3$ remains unknown, although a change in the Fermi surface seems to be a likely origin. High-field measurements on high-quality crystals are needed to further explore the underlying physics.

C. Hall mobility

We finally turn our attention to the carrier mobility in NdTe$_3$ as extracted from Hall measurements. An approximate description of the magnetotransport properties is obtained through a two-band model [Eqs. (3) and (4)] fitted to the antisymmetrized Hall resistivity (Fig. 7). In this model, all electron and hole bands are described collectively as one band, respectively. This holds the advantage of fewer parameters
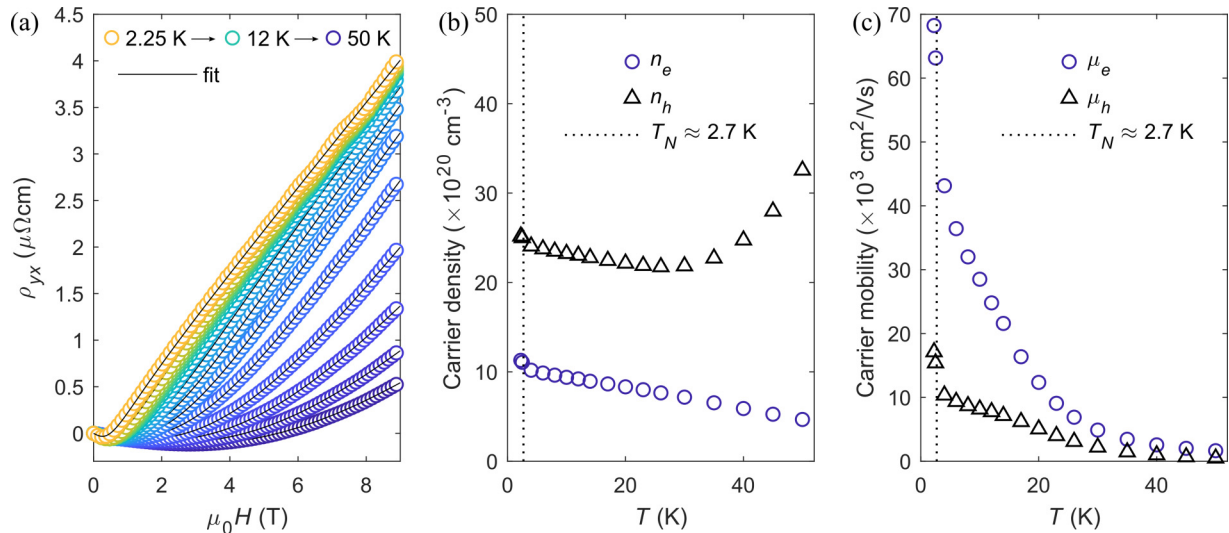
FIG. 7. (a) Hall resistivity of sample S2 at multiple temperatures. The black lines are two-band model fits and the colored circles are data points. (b) Carrier concentrations n, and (c) carrier mobilities μ for electrons (subscript e) and holes (subscript h) extracted from the two-band model fits. The vertical dashed line indicates the Néel temperature.

and higher robustness of the fit, compared to multiple-band models.

In S2, at 2.25 K, the electron and hole concentration is $n_e = 1.1 \times 10^{21}$ cm^{-3} and $n_h = 2.5 \times 10^{21}$ cm^{-3}, respectively, and the mobility is $\mu_e = 68\,000$ cm^2/V s for electrons and $\mu_h = 17\,000$ cm^2/V s for holes. We also performed fits to the Hall conductivity (Fig. S9(b) [19]). The carrier concentrations from the Hall conductivity at 2.5 K are $n_e = 9.9 \times 10^{20}$ cm^{-3} and $n_h = 2.4 \times 10^{21}$ cm^{-3}, and the mobilities are $\mu_e = 56\,000$ cm^2/V s and $\mu_h = 22\,000$ cm^2/V s. The mobilities obtained from the two methods can be considered boundary values within which the real mobility is found.

A ratio of the Hall mobility versus the quantum mobility for the individual pockets is related to the impact of scattering. The ratio μ_t/μ_q, which is about a factor of 10 in this study, suggests a reduced back-scattering process [28].

The transport mobilities in NdTe$_3$ match the high values reported for GdTe$_3$ [9]. Such high carrier mobilities are quite remarkable for magnetically ordered materials and they seem to reflect a general property of the RTe$_3$ family. In fact, a high transport mobility of 3×10^4 cm^2/V s was also reported for nonmagnetic LaTe$_3$ [25]. The delocalized chemical bonds in the Te square nets may be the cause, as they should facilitate efficient transport, similarly as in graphene [1]. Although rare-earth tritellurides undergo CDW transitions at high temperature, the Fermi surface is only partially gapped, pointing to the maintenance of delocalized chemical bonds in the system.

The mobility in NdTe$_3$ is significantly enhanced below the magnetic-ordering temperature. This feature is consistent for all three samples (Sec. SII.D of the SM [19]) and in line with the simultaneous resistivity drop [Fig. 1(d), inset]. In prior measurements on GdTe$_3$, we also observed a signature of mobility enhancements below T_N [9]; however, the enhancement is much more dramatic in NdTe$_3$ with a 58% increase from 4 K to 2.25 K in S2 for electrons. One could speculate that the high mobility is linked to the delocalized chemical bonds and that, therefore, high-mobility magnets can be achieved in

materials with such bonds. Further low-temperature studies may be of value to explore this effect.

As a final note, it may appear that the carrier density slightly increases below the Néel temperature in Fig. 7(b). However, this feature is not consistent among all probed samples and may therefore not be related to the mobility enhancement.

IV. CONCLUDING REMARKS

We have reported the low-temperature transport properties of NdTe$_3$ investigated by means of quantum oscillations on high-quality crystals. In particular, SdH oscillations from three different samples reveal peculiar features. The amplitude originating from the small α pocket has an anomalous behavior below the Néel transition, which differs among the samples. An even more puzzling anomaly at higher temperature implies significant cyclotron mass changes and has highly sample-quality dependent characteristics. We also resolved that the α pocket is composed of multiple frequencies. Our findings stress the importance of high crystal quality and a thorough examination of multiple samples.

Furthermore, the low-temperature Hall-transport mobilities are very high in all probed samples. It seems that delocalized chemical bonds facilitate high mobility in samples with magnetic order, opening a door for high-mobility magnetic devices.

[1] S. Klemenz, A. K. Hay, S. M. L. Teicher, A. Topp, J. Cano, and L. M. Schoop, The role of delocalized chemical bonding in square-net-based topological semimetals, J. Am. Chem. Soc. **142**, 6350 (2020).

[2] L. M. Schoop, F. Pielnhofer, and B. V. Lotsch, Chemical principles of topological semimetals, Chem. Mater. **30**, 3155 (2018).

[3] K. I. Bolotin, K. J. Sikes, Z. Jiang, M. Klima, G. Fudenberg, J. Hone, P. Kim, and H. L. Stormer, Ultrahigh electron mobility in suspended graphene, Solid State Commun. **146**, 351 (2008).

[4] W. Luo and H. Xiang, Room temperature quantum spin Hall insulators with a buckled square lattice, Nano Lett. **15**, 3230 (2015).

[5] R. Lou, J.-Z. Ma, Q.-N. Xu, B.-B. Fu, L.-Y. Kong, Y.-G. Shi, P. Richard, H.-M. Weng, Z. Fang, S.-S. Sun, Q. Wang, H.-C. Lei, T. Qian, H. Ding, and S.-C. Wang, Emergence of topological bands on the surface of ZrSnTe crystal, Phys. Rev. B **93**, 241104(R) (2016).

[6] S. M. Young and C. L. Kane, Dirac Semimetals in Two Dimensions, Phys. Rev. Lett. **115**, 126803 (2015).

[7] S. Pezzini, M. R. van Delft, L. M. Schoop, B. V. Lotsch, A. Carrington, M. I. Katsnelson, N. E. Hussey, and S. Wiedmann, Unconventional mass enhancement around the Dirac nodal loop in ZrSiS, Nat. Phys. **14**, 178 (2018).

[8] C. S. A. Müller, T. Khouri, M. R. van Delft, S. Pezzini, Y.-T. Hsu, J. Ayres, M. Breitkreiz, L. M. Schoop, A. Carrington, N. E. Hussey, and S. Wiedmann, Determination of the Fermi surface and field-induced quasiparticle tunneling around the Dirac nodal loop in ZrSiS, Phys. Rev. Research **2**, 023217 (2020).

[9] S. Lei, J. Lin, Y. Jia, M. Gray, A. Topp, G. Farahi, S. Klemenz, T. Gao, F. Rodolakis, J. L. McChesney, C. R. Ast, A. Yazdani, K. S. Burch, S. Wu, N. P. Ong, and L. M. Schoop, High mobility in a van der Waals layered antiferromagnetic metal, Sci. Adv. **6**, eaay6407 (2020).

[10] C. Haas, Spin-disorder scattering and magnetoresistance of magnetic semiconductors, Phys. Rev. **168**, 531 (1968).

[11] E. DiMasi, M. C. Aronson, J. F. Mansfield, B. Foran, and S. Lee, Chemical pressure and charge-density waves in rare-earth tritellurides, Phys. Rev. B **52**, 14516 (1995).

[12] C. Malliakas, S. J. L. Billinge, H. J. Kim, and M. G. Kanatzidis, Square nets of tellurium: Rare-earth dependent variation in the charge-density wave of RTe_3 (RE = rare-earth element), J. Am. Chem. Soc. **127**, 6510 (2005).

[13] V. Brouet, W. L. Yang, X. J. Zhou, Z. Hussain, R. G. Moore, R. He, D. H. Lu, Z. X. Shen, J. Laverock, S. B. Dugdale, N. Ru, and I. R. Fisher, Angle-resolved photoemission study of the evolution of band structure and charge density wave properties in RTe_3 (R = Y, La, Ce, Sm, Gd, Tb, and Dy), Phys. Rev. B **77**, 235104 (2008).

[14] N. Ru, C. L. Condron, G. Y. Margulis, K. Y. Shin, J. Laverock, S. B. Dugdale, M. F. Toney, and I. R. Fisher, Effect of chemical pressure on the charge density wave transition in rare-earth tritellurides RTe_3, Phys. Rev. B **77**, 035114 (2008).

[15] A. Banerjee, Y. Feng, D. M. Silevitch, J. Wang, J. C. Lang, H.-H. Kuo, I. R. Fisher, and T. F. Rosenbaum, Charge transfer and multiple density waves in the rare earth tellurides, Phys. Rev. B **87**, 155131 (2013).

[16] N. Ru, R. A. Borzi, A. Rost, A. P. Mackenzie, J. Laverock, S. B. Dugdale, and I. R. Fisher, de Haas-van Alphen oscillations in the charge density wave compound lanthanum tritelluride $LaTe_3$, Phys. Rev. B **78**, 045123 (2008).

[17] A. A. Sinchenko, P. D. Grigoriev, P. Monceau, P. Lejay, and V. N. Zverev, Slow oscillations of in-plane magnetoresistance in strongly anisotropic quasi-two-dimensional rare-earth tritellurides, J. Low Temp. Phys. **185**, 657 (2016).

[18] P. Walmsley, S. Aeschlimann, J. A. W. Straquadine, P. Giraldo-Gallo, S. C. Riggs, M. K. Chan, R. D. McDonald, and I. R. Fisher, Magnetic breakdown and charge density wave formation: A quantum oscillation study of the rare-earth tritellurides, Phys. Rev. B **102**, 045150 (2020).

[19] See Supplemental Material at http://link.aps.org/supplemental/10.1103/PhysRevB.102.245109 for additional experimental results, data analysis, and data processing; Refs. [29,30] are cited therein.

[20] N. Ru, J.-H. Chu, and I. R. Fisher, Magnetic properties of the charge density wave compounds RTe_3 (R = Y, La, Ce, Pr, Nd, Sm, Gd, Tb, Dy, Ho, Er, and Tm), Phys. Rev. B **78**, 012410 (2008).

[21] Y. Iyeiri, T. Okumura, C. Michioka, and K. Suzuki, Magnetic properties of rare-earth metal tritellurides RTe_3(R = Ce, Pr, Nd, Gd, Dy), Phys. Rev. B **67**, 144417 (2003).

[22] B. H. Min, J. H. Cho, H. J. Lee, C. W. Han, D. L. Kim, and Y. S. Kwon, Specific heat study in RTe_2 (R: La, Ce, Pr, Sm and Gd), Phys. B: Condens. Matter **281**, 118 (2000).

[23] Ł. Gondek, A. Szytuła, D. Kaczorowski, A. Szewczyk, M. Gutowska, and P. Piekarz, Multiple magnetic phase transitions in $Tb_3Cu_4Si_4$, J. Phys.: Condens. Matter **19**, 246225 (2007).

[24] M. Rotter, M. Tegel, D. Johrendt, I. Schellenberg, W. Hermes, and R. Pöttgen, Spin-density-wave anomaly at 140 K in the ternary iron arsenide $BaFe_2As_2$, Phys. Rev. B **78**, 020503(R) (2008).

[25] A. Pariari, S. Koley, S. Roy, R. Singha, M. S. Laad, A. Taraphder, and P. Mandal, Fascinating interplay between charge density wave order and magnetic field in nonmagnetic rare-earth tritelluride $LaTe_3$, arXiv:1901.08267.

[26] J. Laverock, S. B. Dugdale, Z. Major, M. A. Alam, N. Ru, I. R. Fisher, G. Santi, and E. Bruno, Fermi surface nesting and charge-density wave formation in rare-earth tritellurides, Phys. Rev. B **71**, 085114 (2005).

[27] B. K. Norling and H. Steinfink, The crystal structure of neodymium tritelluride, Inorg. Chem. **5**, 1488 (1966).

[28] T. Liang, Q. Gibson, M. N. Ali, M. Liu, R. J. Cava, and N. P. Ong, Ultrahigh mobility and giant magnetoresistance in the Dirac semimetal Cd_3As_2, Nat. Mater. **14**, 280 (2015).

[29] A. Audouard and J.-Y. Fortin, Does Fourier analysis yield reliable amplitudes of quantum oscillations? Eur. Phys. J.: Appl. Phys. **83**, 30201 (2018).

[30] J. Hu, S.-Y. Xu, N. Ni, and Z. Mao, Transport of topological semimetals, Annu. Rev. Mater. Res. **49**, 207 (2019).